Energy 283 (2023) 128455

Contents lists available at ScienceDirect

Energy

journal homepage: www.elsevier.com/locate/energy

Experimental dynamic load cycling and current density measurements of different inlet/outlet configurations of a parallel-serpentine PEMFC

Christian Suárez [a,b,*], Baltasar Toharias [a], María Salva Aguirre [a], Artem Chesalkin [c], Felipe Rosa [a], Alfredo Iranzo [a,b]

[a] Thermal Engineering Group, Energy Engineering Department, School of Engineering, University of Seville, Spain
[b] AICIA, Andalusian Association for Research & Industrial Cooperation, Spain Camino de los Descubrimientos s/n, 41092, Seville, Spain
[c] ENET Centre – Research Centre of Energy Units for Utilization of Non Traditional Energy Sources, VSB Technical University of Ostrava, Czech Republic

ARTICLE INFO

Handling Editor: A. Olabi

Keywords:
Polymer electrolyte membrane fuel cell
Dynamic load cycling
Current density mapping

ABSTRACT

Proton-exchange membrane fuel cells (PEMFCs) in the transport sector require specific design and durability, and stable and reliable performance under varying cycling loads. In this study, experimental dynamic load cycling (DLC) tests and current density mapping (CDM) measurements of local current densities and temperatures were performed for different inlet/outlet configurations of reactants in a parallel-serpentine PEMFC. Results were analyzed in terms of the polarization and power curves and the DLC tests, indicating that the Inverse Hydrogen Flow configuration performed best. However, the differences with respect to the other inlet/outlet configurations (Normal Flow, Inverse Air Flow and Inverse Flow) were not significant with maximum relative voltage and power densities differences below 5% in the polarization and power curves. Also results of the experimented inlet/outlet configurations during the DLCs were similar, with maximum differences in terms of energy during the cycle below 10% comparing the best configuration (Inverse Hydrogen Flow) with the worst. CDM measurements showed an inverse bell-shaped distribution with higher current density values in the external part of the bipolar plate and lower values in the central part and a highly homogeneous temperature distributions in all configurations.

1. Introduction

Currently, there is a high demand for propulsion systems supported by renewable energy sources in the transport sector, one of them being PEMFCs. Due to their zero-emission properties, high efficiency and low operating temperature, fuel cells are a good alternative, and they have become a potential substitute for conventional combustion engines [1]. The operating conditions of PEMFCs in the transport sector require specific design and durability, and stable and reliable performance under changeable and cycling loads. A number of studies have focused on the performance or durability during PEMFCs operation at different loads, without accent on the PEMFC specific urban cycle dynamic load [2–5]. The degradation mechanisms associated with the start-up and shut-down of PEMFCs for specific automotive applications requires future design investigations on the way to improve PEMFCs performance and stable operation in urban mode [6,7]. The PMFCs degradation and performance improvement must be first studied at membrane electrode assembly (MEA) level before any scale-up to stack and system levels, while state-of-the-art MEAs are sometimes observed to be suffering from insufficient reliability and stability under certain conditions [8–10].

One of the key components in PEMFCs are the bipolar plates (BPs) as they represent a significant part of the volume, weight and cost [11,12]. The material and design of the channels in the BPs have to ensure an appropriate water management within the cell and improve the performance of the cell at high current densities [13]. Such materials could include graphite, coated metallic or composite plates [14,15]. Alternatively, BPs improvement could be done via different flow field designs such as parallel, serpentine, parallel-serpentine and as well bioinspired designs [16,17]. Effect of BPs material and flow field design on PEMFCs

Abbreviations: BP, bipolar plate; CDM, current density mapping; DLC, dynamic load cycling; FC, fuel cell; GDL, gas diffusion layer; IAF, inverse air flow; IF, inverse flow; IHF, inverse hydrogen flow; JRC, joint research centre; NEDC, new European driving cycle; NF, normal flow; OCV, open circuit voltage; PEM, proton-exchange membrane; PEMFC, proton-exchange membrane fuel cell; PID, proportional integral derivative.

* Corresponding author. Thermal Engineering Group, Energy Engineering Department, School of Engineering, University of Seville, Spain.
E-mail address: chss@us.es (C. Suárez).

https://doi.org/10.1016/j.energy.2023.128455
Received 26 October 2022; Received in revised form 27 June 2023; Accepted 15 July 2023
Available online 20 July 2023

performance have been studied in a significant number of researches, and the state of the art in this field has been summarized in the review works by Hermann A. et al. [18], Zhang S. et al. [19], Wang Y. et al. [20], Wang J [21]. and Porstmann S. et al. [22].

Analyzing the local distributions of both current density and temperature fields during variable load operation is important for a better understanding of PEMFC behaviour, efficiency and possible points for future improvements in the design of the BP. Previous works have studied the design of BP channels by measuring the polarization curve [23]. A number of studies also analyzed the local phenomena from sensors that measure the current density and temperature distribution within the cell [24–29]. In researches [24–27], these distributions were analyzed along the reactant gas flow direction and also across lateral directions through land and channel areas, concluding that local measurements of current densities and temperatures could provide critical information to optimize flow field design and fuel cell performance. Different local conditions may exist in PEMFCs that lead to an inhomogeneous distribution of current and heat. Current density distribution and the FC performance homogeneity demonstrated high sensitivity to small humidity changes and dry-out phenomena in PEMFC stacks [28] and that increasing the cathode stoichiometry can effectively improve the uniformity of current density distribution, and mitigate the local oxygen starvation, especially at high FC loads [29].

A number of previous studies on cold start and dynamic FC loading [10,30–34] show the importance of the future investigation of PEMFC performance and durability improvement. Cold start is a critical condition in FCs automotive application where FCs operation related to the dynamically changeable load. The study of Jiao K [30]. investigates the cold start characteristics of a PEMFC through the simultaneous measurements of current and temperature distributions. For both the failed and the successful cold start processes, the highest temperature is initially near the inlet region of the cell, and is also in the middle region after the overall peak current density is reached. The PEMFC lifetime prediction through load and potential cycling accelerated degradation was described by Choi S.R. et al. [31].

Han J. et al. [32] found that even at very low current densities (0.52 A/cm^2) for the full dynamic cycling load conditions, significant FC performance degradation has been observed, especially by voltage degradation at high temperatures. Wang Y. et al. [33] investigated that increase in the current density leads to anode drying due to electro-osmotic resistance, while it takes several seconds for water back-diffusion and anode humidified gas to rewet the anode side of the polymer membrane. Mayur M. et al. [34] modelled a PEMFC performance and durability for a virtual FC car. The work demonstrated FC durability analysis due to membrane degradation under highly dynamic load levels changes of the New European Driving Cycle (NEDC) and identified critical cell loading regions imposed by the NEDC FC operation.

From the above literature review, it is clear that previous related studies have focused on the analysis of local distributions of current densities and temperatures for different flow channel's designs and operating conditions, as well as on the performance and durability during dynamic load cycling tests. However, as far as we are concerned, no previous research has investigated the evolution of local distributions of current densities and temperatures during the PEMFC urban cycle operation. In the present work, this novelty is presented, and the experimental methodology followed to examine the PEMFC performance under operating and stress conditions for automotive applications described by the European Commission in the JRC Science Policy Report [35]. Current density and temperature distribution were experimentally measured for four different inlet/outlet configurations of a parallel-serpentine cross-flow PEMFC, and performance results were analyzed and compared.

2. Materials and experimental procedure

The materials and the experimental procedure followed in this research are summarized in this section.

2.1. Materials

The experimental work was performed with a PEM fuel cell test station, dedicated to experimental testing of PEM single cells and short stacks up to 500 W. The test environment shown in Fig. 1 (a) represents a typical fuel cell test bench, with a reactant gas handling unit including humidifiers, a heating and cooling system controlled by a PID mechanism using film heaters and air fans, and an electronic load.

The current density mapping sensor shown in Fig. 1 (b) was used to measure the current density and temperature distributions inside the fuel cell. With a relatively small thickness of 0.7 mm, the CDM sensor was inserted between the bipolar cathode plate and the cathode current collector. The sensor was manufactured ad hoc for the ElectroChem fuel cell, thus having the same active area, and provided a uniformly distributed sequence of measurements in an 18 × 18 matrix for current density and a 9 × 9 matrix for temperature during the experiments.

The parallel-serpentine flow field design of an approximately 50 cm^2 (width: 69.8 mm, height: 69.9 mm) active area ElectroChem Inc. PEM fuel cell, with 9.5 mm thick graphite bipolar plates for both anode and cathode, was experimentally investigated in this work. The flow field consisted of five parallel serpentine channels connected by manifolds at the end of each pass, see Fig. 2. The reactants flow from the inlet located at one corner of the bipolar plate and are directed through the parallel serpentine channels to the outlet located at the opposite corner. The channel geometry had a width of 0.71 mm, a height of 1.1 mm, and a rib width of 0.86 mm. The collector channels were 1.5 mm width and 1.7 mm height. Surface roughness measurements using high-precision 3D optical profilers based on confocal and interferometry showed a value of Ra = 0.227 μm for the graphite bipolar plates.

The anode and cathode arrangements and a schematic diagram of the parallel-serpentine channels of the bipolar plates are shown in Fig. 2. While the anode parallel-serpentine channels were arranged horizontally as depicted in Fig. 2 (a), the cathode bipolar plate channels were arranged vertically as shown in Fig. 2 (b). This vertical arrangement was preferred in the cathode plate to facilitate water removal by gravity and to avoid the horizontal configuration for the cathode, which is more prone to water flooding.

Bipolar plates were tightened with end plates to a value of 5 Nm using a torque wrench, bolts and nuts to prevent leakage and for uniform current collection, with the anode positioned over the cathode in the direction indicated by the arrow in Fig. 2 (a) and (b). A cross flow in which the anode (red color) and cathode (blue color) flow channels are perpendicular, as depicted in Fig. 2 (c). To clarify the location of reactants inlet and outlet and the way anode and cathode flow channels are positioned, a schematic diagram of the reactants flow directions for the anode, the cathode and their intersections are shown in Fig. 2 (d), Fig. 2 (e) and Fig. 2 (f) respectively. In these diagrams, only the central channel of the five parallel channels in each pass of the serpentine is represented with black color to better visualize the reactants flow directions.

2.2. Experimental procedure

Experimental measurements were performed using a PEM fuel cell test station to obtain the polarization and power curves of each inlet/outlet configuration. The power equipment included a programmable direct current load from Adaptive Power Systems, with an accuracies of 0.025%, 0.1%, and 0.125% for voltage, current and power measurements, respectively. Fuel cell dynamic load cycle (FC-DLC) tests were also performed, to simulate the voltage and current density during a real driving cycle. During all experiments, current density and temperature

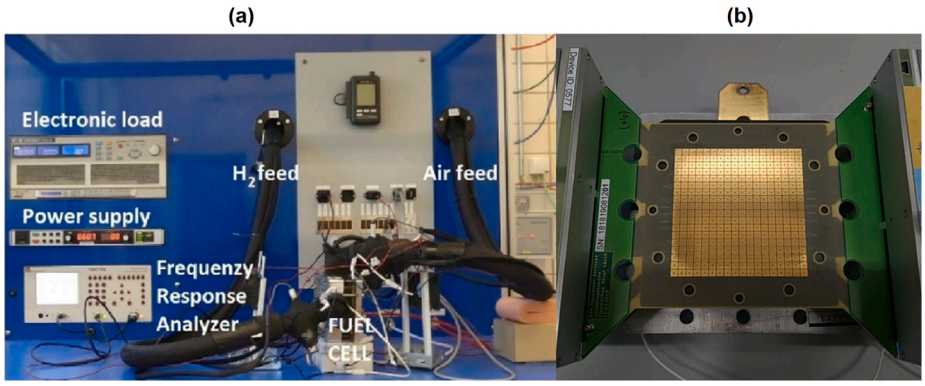

Fig. 1. Fuel cell test station (a) and CDM sensor (b).

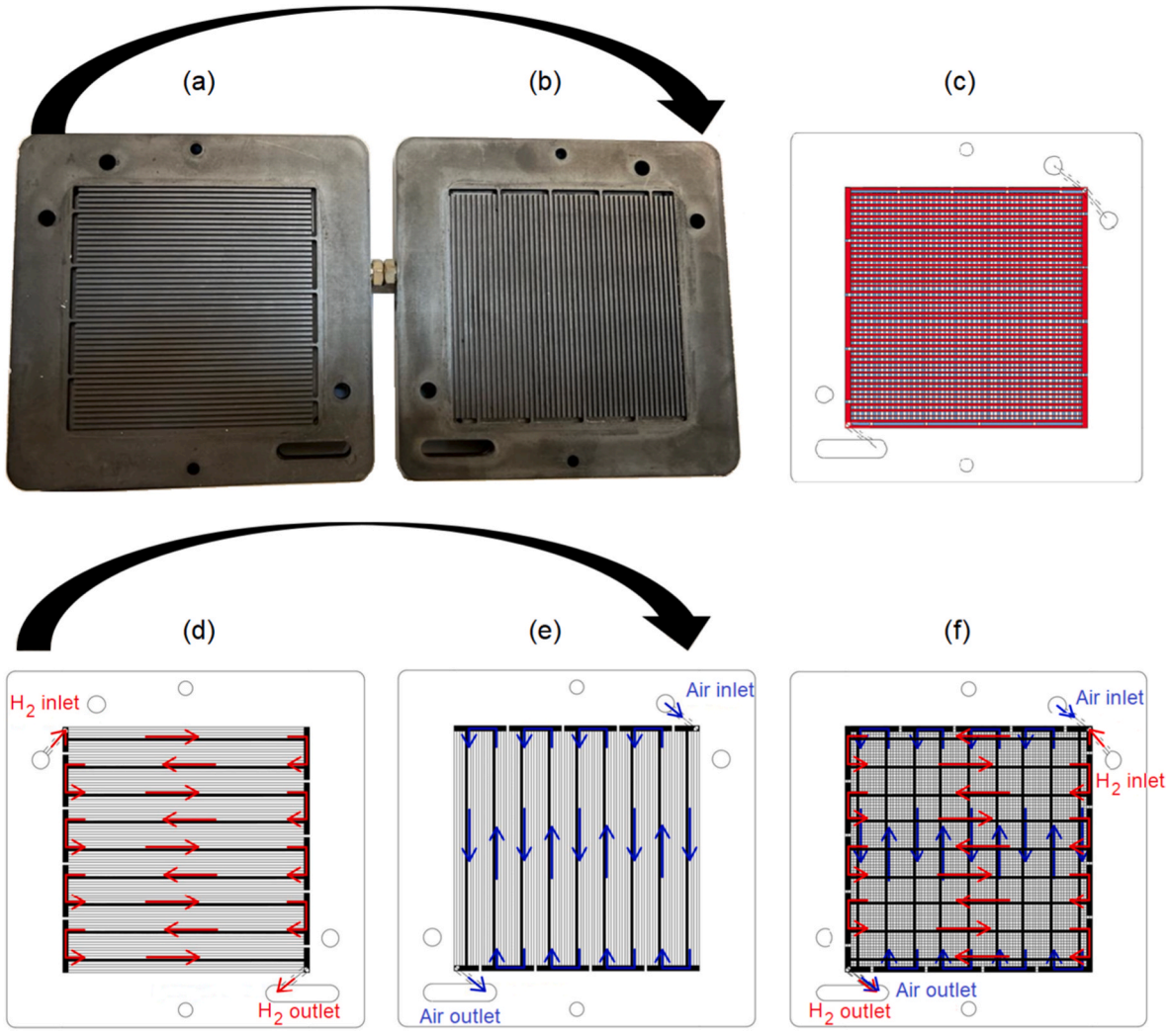

Fig. 2. Bipolar plate channels flow: (a) ElectroChem anode, (b) ElectroChem cathode, (c) Resulting cross-flow distribution, (d) Schematic anode flow directions, (e) Schematic cathode flow directions and (f) Schematic cross-flow distribution.

distribution data were collected using the CDM sensor provided by S++ Simulation Services [36] with a data acquisition rate of 1 s and a resolution of voltage, temperature and current variables of 1.5 mV, 0.1 °C and 0.001% of the measured current, respectively.

In order to analyze only the effect of the inlet/outlet reactants configurations on fuel cell performance, fuel cell operating conditions were kept fixed at typical operating values throughout all tests, as summarized in Table 1. Cell temperature and relative pressure were set at 65 °C and 0.5 bar respectively. Intermediate anode and cathode relative humidities of 60% were considered during the experiments, to avoid potential problems of membrane dehydration at very low relative humidities or water flooding at very high relative humidities. Anode and cathode stoichiometric factors were set at 1.3 and 2.5 respectively, with hydrogen and air inlet mass flow values of 0.457 NL/min and 2.140 NL/min for a representative operating condition of 1 A/cm^2 current density.

Table 1
Fuel cell reference operating conditions.

Operating condition	Value
Cell temperature (°C)	65
Cell relative pressure (bar)	0.5
Anode and cathode relative humidity (%)	60
Anode stoichiometric factor (−)	1.3
Cathode stoichiometric factor (−)	2.5

2.2.1. Inlet/outlet flow-field configurations

Four flow configurations were analyzed by changing the relative inlets and outlets positions of the reactants, as shown in Fig. 3: Normal Flow (NF), Inverse Air Flow (IAF), Inverse Hydrogen Flow (IHF) and Inverse Flow (IF). In the NF configuration, the reactants inlets and outlets were connected according to the original ElectroChem fuel cell design. The other three configurations were chosen to investigate the potential for improving fuel cell performance by using other suitable inlet/outlet positions that did not involve any additional materials or operation costs. In the IAF configuration, the air inlet and outlet were reversed while the hydrogen flow was maintained in its normal configuration. Similarly, in the IHF configuration, the hydrogen inlet and outlet were inverted while the air flow was maintained in its normal configuration. Finally, in the IF configuration, both the air and hydrogen flows, were inverted.

Considering the geometry of the parallel serpentine flow field design and the inlet mass flow values for a representative operating condition of a 1 A/cm^2 current density, laminar flow with relatively low values of pressure drop and velocities were obtained within the four configurations considered.

An exploded view drawing with the description of the primary components and complete assembly are shown in Fig. 4 (a) and (b) respectively, where it can be observed that the CDM sensor was positioned on the cathode side, between the bipolar plate and the current collector. Experimental setup for the NF configuration is also shown in Fig. 4 (c), where the positions of the inlet/outlet can be observed. Insulated air (black color) and hydrogen (grey color) inlet connectors, feed the fuel cell in the upper right corner while non-reactant gases are extracted through the air (blue color) and hydrogen (red color) outlet pipes.

2.2.2. Polarization and power curves

Polarization and power curves were obtained according to the Joint Research Centre (JRC) protocol for the different proposed configurations [35]. Each test started with preconditioning of the cell by setting the operating conditions to the specified operating condition values. To reach these conditions, the cell current density was gradually increased in steps of 0.1 A/cm^2 until a voltage of 0.5 V was reached. This current density was kept constant 3600 s to stabilize the conditions. The cell was then placed under OCV (Open Circuit Voltage) conditions for a period of 90 s. The measurement of these curves was performed in galvanostatic mode, starting from the OCV voltage and using fixed current density steps as indicated in the JRC protocol [35]. The polarization curve was divided into two curves, the first from the current density of 0 A/cm^2 (OCV) to maximum current density, and the second from the maximum current density to OCV. This test was repeated three times to analyze the reproducibility of the results and to obtain a better reliability of the data. The data acquisition rate of the test bench is 1 s, so the average of the last 30 values was used to post-process of the data. After processing the data, the polarization and power curves were plotted for each reactants flow configuration. Simultaneously with the acquisition of the polarization

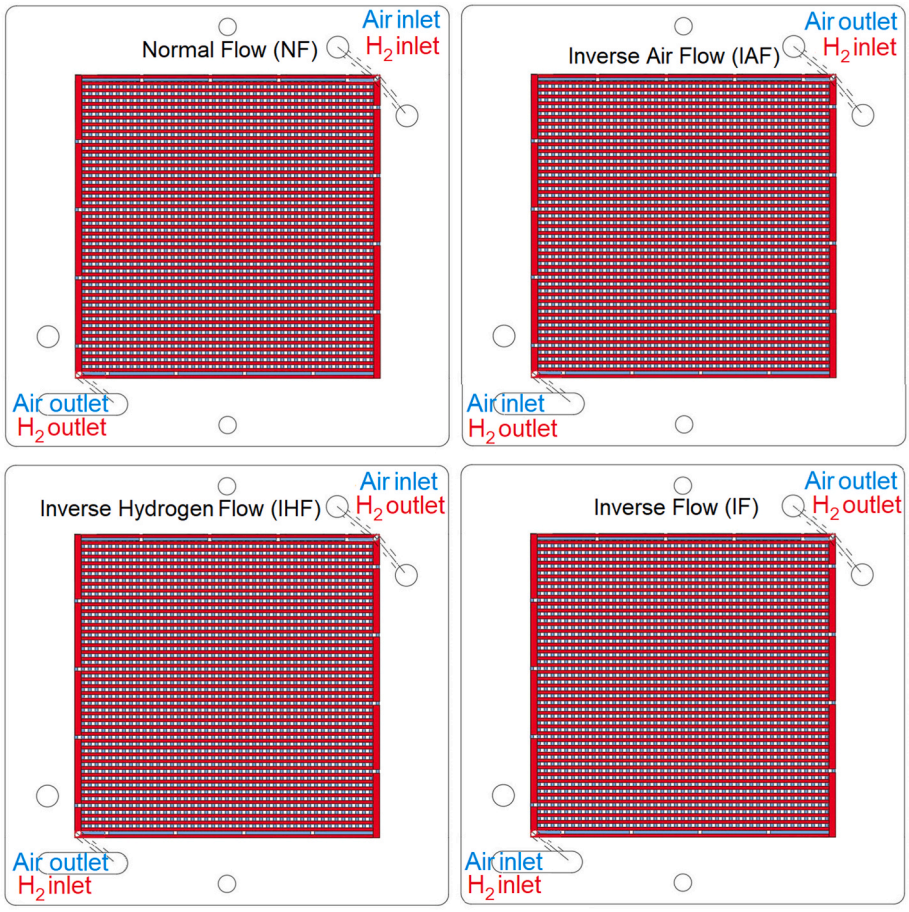

Fig. 3. Inlet/outlet configurations.

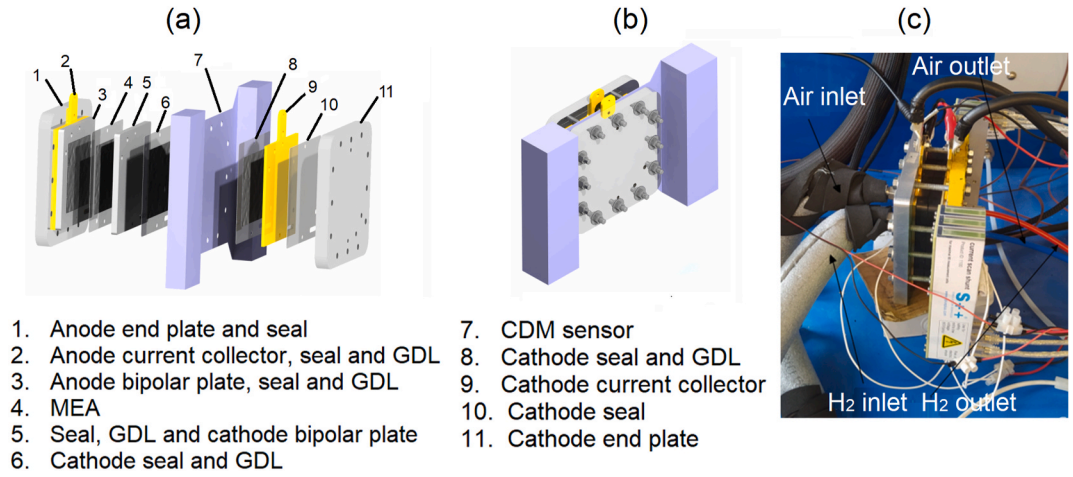

Fig. 4. Experimental setup for Normal Flow configuration (NF).

and power curves, the electro-thermal mapping instrument was used to measure and collect the current density and temperature data at an acquisition rate of 1 s.

2.2.3. FC-DLC test

The objective of the FC-DLC test in this work was to subject the fuel cell to repetitive load cycles and measure the effect of the different periods of acceleration, braking and constant speed had on the current density and temperature fields within the fuel cell. During the tests, the current density is varied according to the established dynamic load cycles depicted in Fig. 5 and the voltage is obtained. The current density ratio was defined as a percentage of the maximum current density value. The cycle consisted of four repetitions of 195 s each at a low speed, such as that used on urban roads (urban driving cycle zone), followed by a period of 400 s simulating a highway condition and its corresponding acceleration (extra urban driving cycle zone). The complete cycle would correspond to a distance of approximately 11 km driven for 20 min.

3. Results and discussion

In this section, the main results of the experimental research are presented and discussed.

3.1. Polarization curves and CDM measurements

In a first set of experiments, polarization and power curves, including CDM measurements, were performed for the four different inlet/outlet configurations (NF, IAF, IHF and IF). The polarization curves results were also used to define the 100% current load for each configuration in the subsequent DLC tests.

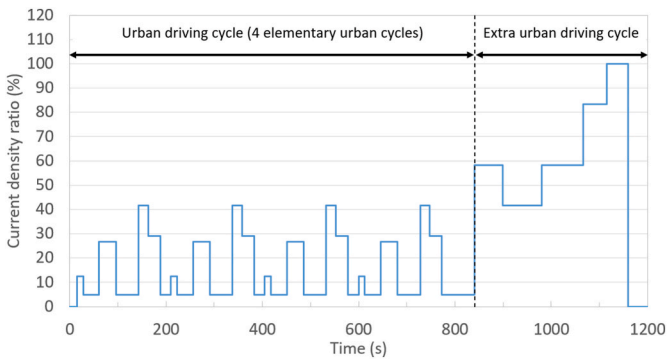

Fig. 5. Fuel cell dynamic load cycle [35].

3.1.1. Polarization and power density curves

Polarization and power curves were obtained following the experimental procedure described in section 2.2.2, and a comparison of the results for the different configurations was depicted in Fig. 6. Ascending (from open circuit voltage to maximum current) and descending (from maximum current to open circuit voltage) curves were included for each configuration.

The experimental results indicated that the hysteresis phenomenon was present in all the studied configurations, as the forward curve (increasing current) was below the backward curve (decreasing current), suggesting that there was a certain degree of drying in the cell.

The polarization curve in each case also showed the three polarization regions (activation, ohmic, and mass transport). Similar voltage and power densities were obtained in the region of activation losses for density current values below 0.2 A/cm^2. For example, at a current density of 0.1 A/cm^2, the difference in voltage between the best configuration NF and the worst configuration IHF was only about 0.02 V. The four configurations also performed similarly in this region in terms of power densities, with negligible differences. However, in the ohmic losses region, where the cell potential decreases approximately linearly with the current, the IHF configuration performed better, obtaining the highest voltage with higher values of approximately 0.02 V compared to the worst IF and NF configurations at a density current value of 0.7 A/cm^2. For the same density current value higher relative power densities of 3–4% were obtained for the IHF configuration. The IHF configuration performed even better in the region of mass transport losses, where the cell potential drop deviates from the linear relationship with current density due to a more pronounced concentration polarization, with higher voltage values in the range of 0.02–0.03 V compared to the other configuration NF. The same behavior was observed when comparing the power curves, in which the IHF configuration achieved higher power densities compared to the other configurations. However, these differences were small, with relative power density differences in the range of 3–5% at a current density of 0.9 A/cm^2.

Representative values of the average current densities in the polarization curves, obtained as the average between the ascending and descending curves, were later used in the FC-DLC tests to define the respective 100% current load values. In particular, for a representative voltage value of 0.6 V, the experimental current density of IHF configuration was 0.898 A/cm^2 (44.90 A), a 14.4% higher than the worst case of the NF configuration with 0.785 A/cm^2 (39.25 A). The IF and IAF configurations achieved similar average current density at 0.6 V of 0.810 A/cm^2 (40.5 A) and 0.820 A/cm^2 (40.1 A) respectively. Although the IHF configuration performed best, the maximum current density achieved was the lowest (0.90 A/cm^2), compared to the 1.04 A/cm^2 achieved by the IAF configuration.

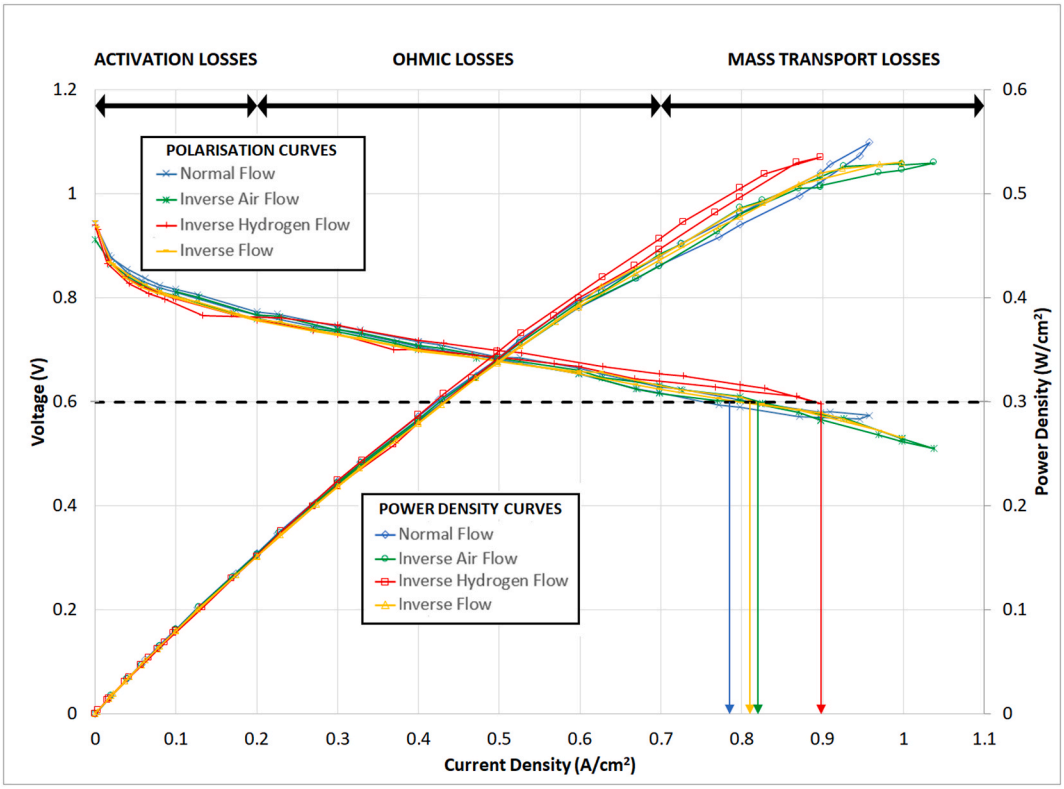

Fig. 6. Polarization and power curves for the different configurations Normal Flow (NF), Inverse Air Flow (IAF), Inverse Hydrogen Flow (IHF) and Inverse Flow (IF).

The main results described above for the polarization and power curves are summarized in Table 2, which shows the average current density at 0.6 V, the maximum current densities achieved and the maximum power densities at 0.9 A/cm^2 are shown for the four configurations studied.

3.1.2. CDM measurements

During the experimental acquisition of the polarization curves of each configuration, CDM measurements were performed with a data acquisition rate of 1 s.

Figs. 7 and 8 show a comparison of the CDM results for a current density of 0.4 A/cm^2 (20 A) as a representative illustration of the current density and temperature distributions obtained.

Regarding the current density, similar variations were obtained for the different configurations, observing an inverse bell-shaped distribution with higher values in the outer part of the bipolar plate and lower values in the central part regardless of the inlet/outlet positions. Due to the cross-flow configuration of the anode and cathode channels, the higher current densities were obtained in the collector channels, where the interception of the anode and cathode channels is much higher compared to the parallel-serpentine channels traversing the central part of the bipolar plate. In addition, the larger width and height dimensions of the collector channels allowed higher reactant mass flow rates in these zones, resulting in higher local current densities.

Very homogeneous distributions of local temperatures were observed for the different configurations. The temperatures measured with the CDM sensor were 2-3 °C higher than the cell temperature operating condition of 65 °C, due to the fact that the cell temperature thermocouple was placed at a more distant position from the GDL, where heat generation occurs during the exothermic reaction.

Similar distributions were obtained for the other current densities studied (0.2 A/cm^2, 0.7 A/cm^2 and 0.9 A/cm^2).

To quantify the degree of homogeneity of current density and temperature, the following variables were defined for current density (I_d) and temperature (T): average (avg), standard deviation (std) and maximum relative deviation (rel, max):

$$I_{d,avg}\left(A/cm^2\right) = \frac{\sum_{i=1}^{i=18\times18} I_d(i)}{18\times18} \tag{1}$$

$$I_{d,std}\left(A/cm^2\right) = \sqrt{\frac{1}{18\times18}\sum_{i=1}^{i=18\times18}\left(I_d(i)-I_{d,avg}\right)^2} \tag{2}$$

$$I_{d,rel,max}(\%) = max\left[\frac{abs\left(I_d(i)-I_{d,avg}\right)}{I_{d,avg}}\cdot 100\right] \tag{3}$$

$$T_{avg}(^\circ C) = \frac{\sum_{i=1}^{i=9\times9} T(i)}{9\times9} \tag{4}$$

$$T_{std}(^\circ C) = \sqrt{\frac{1}{9\times9}\sum_{i=1}^{i=9\times9}\left(T(i)-T_{avg}\right)^2} \tag{5}$$

$$T_{rel,max}(\%) = max\left[\frac{abs\left(T(i)-T_{avg}\right)}{T_{avg}}\cdot 100\right] \tag{6}$$

Note that while the CDM sensor provides 324 local current density measurements evenly distributed in a matrix of 18 × 18 locations, the sensor provides only 81 temperature measurements distributed in a matrix of 9 × 9 locations.

The results of the CDM statistic for current density and temperature are summarized in Table 3 and Table 4, respectively. For current density, it was found that for each configuration an approximately linear increase of the standard deviation with current density. Almost constant heterogeneities were observed for the different intensities, with lower values of 88.7% of the maximum relative deviations from the mean for the IF configuration compared to the others, which remained in the

Table 2
Summary of polarization and power curve results for the four configurations.

Configuration	I_{avg} (A/cm^2)	I_{max} (A/cm^2)	P_{max} (W/cm^2)
NF	0.785	0.960	0.520
IAF	0.810	1.040	0.517
IHF	0.898	0.900	0.535
IF	0.820	1.000	0.520

range of 90.5–91.0%.

In terms of temperatures, an approximately linear decrease of average temperatures with current density was observed in all configurations. The cooling effect due to the increase in reactants mass flow at a lower operating temperature of 65 °C had a greater effect on the average cell temperature than the increase in heat generation at higher current density values. An approximately linear increase of the temperature standard deviation with current density was also observed for each configuration. The maximum relative deviations from the average temperature were very low, less than 1.5% even for the higher case (IHF configuration).

3.2. FC-DLC tests and CDM measurements

In a second set of experiments, DLC tests were performed, including CDM measurements. FC-DLC tests were performed for the four proposed configurations, repeatedly subjecting the cell to the same load cycle, including fast variations in load, prolonged OCV exposure as well as periods of steady-state operation as described in section 2.2.2. During the DLC tests, CDM measurements of current density and temperature were recorded simultaneously every second.

3.2.1. FC-DLC tests

Three load cycles were repeated sequentially for each configuration, taking into account a stabilization period of 1 h before each cycle. The 100% current density references were defined according to the values previously obtained in Table 2: 0.96, 1.04, 0.90 and 1.00 A/cm^2 for the NF, IAF, IHF and IF configurations respectively.

Similar voltage results were obtained in each repetition, with relative differences of less than 1% with respect to the average of the three repetitions. As a representative example, Fig. 9 shows the three repetitions of the DLC test were shown for the IHF configuration. Small voltage variations were observed during the stabilization period prior to each DLC cycle at 0.678 A/cm^2.

A comparison of the FC-DLC tests for the different configurations is shown in Fig. 10 in terms of voltage. For simplicity, the average of the three repetitions in each experiment are shown, starting from t = 0 s.

The four proposed configurations were able to complete the DLC tests with a correct cell response behaviour.

In the range of the urban driving cycle, two different characteristic zones were observed. In a first zone, during the first 60 s, a transient stabilization behavior was observed for all configurations, with an approximately linear increase in current density and an approximately linear decrease in voltage. This initial behavior was due to the initial current density ratios defined in the DLC test, in which the current

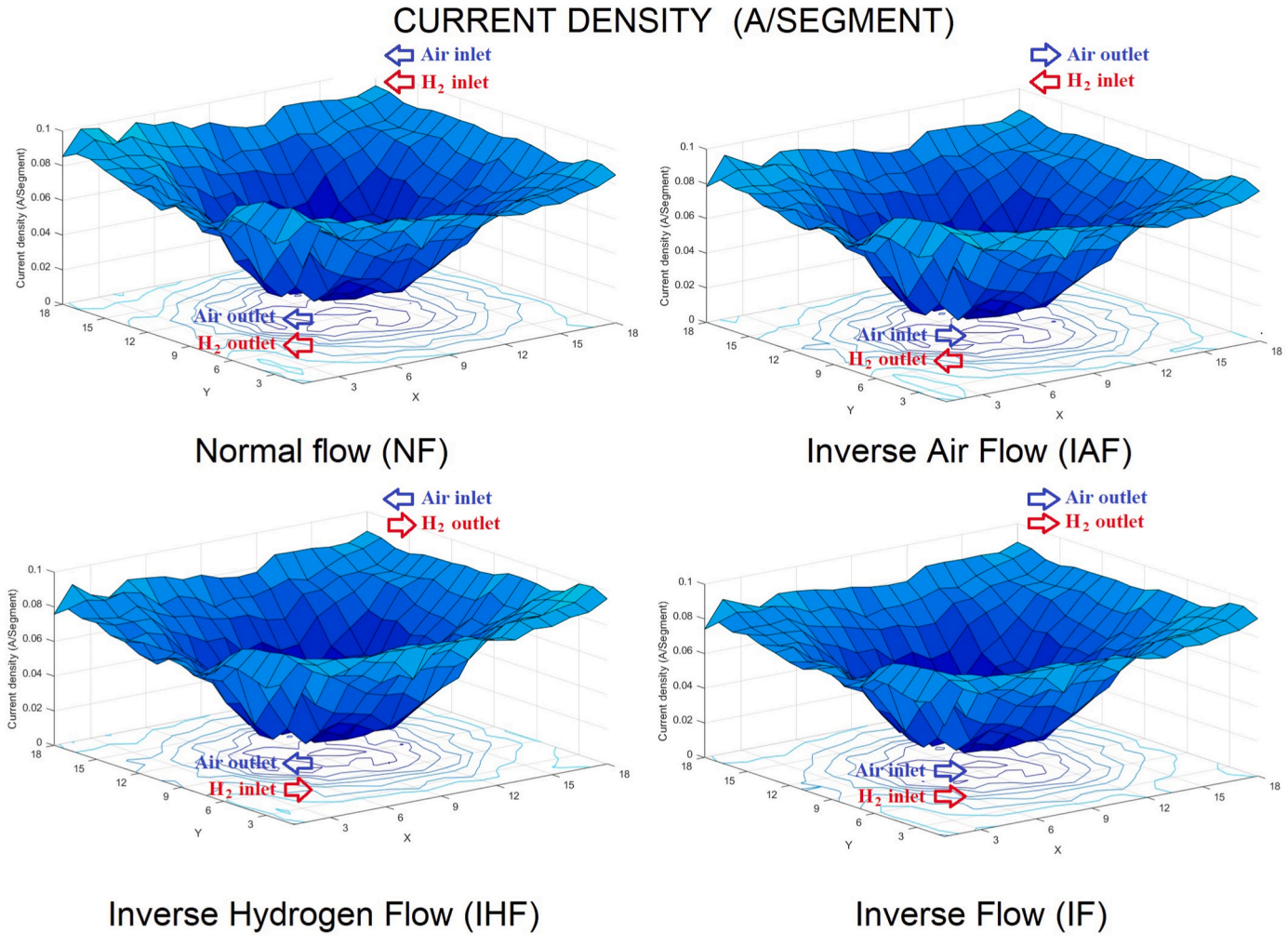

Fig. 7. CDM measurements for current density at 0.4 A/cm^2 (20 A).

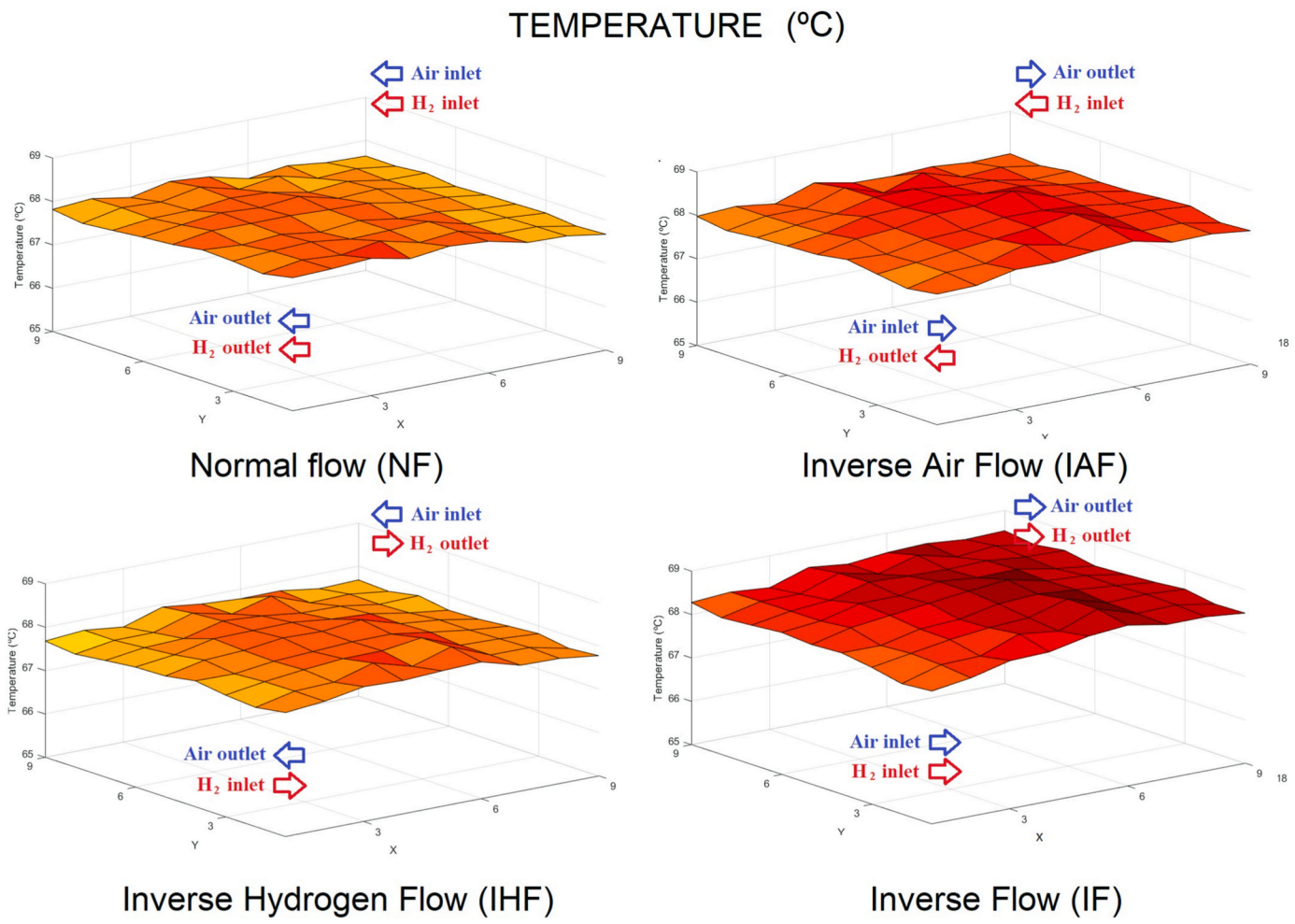

Fig. 8. CDM measurements for temperature at 0.4 A/cm^2 (20 A).

Table 3
Statistical current density results for each configuration. Current density values for 0.2 A/cm^2, 0.4 A/cm^2, 0.7 A/cm^2 and 0.9 A/cm^2, separated by commas for each parameter.

Configuration	$I_{d,avg}$ (A/cm^2)	$I_{d,std}$ (A/cm^2)	$I_{d,rel,max}$ (%)
NF	0.031, 0.062, 0.108, 0.139	0.012, 0.024, 0.042, 0.054	90.6, 90.6, 90.6, 90.5
IAF	0.031, 0.062, 0.108, 0.139	0.012, 0.023, 0.041, 0.053	90.7, 90.6, 90.9, 90.7
IHF	0.031, 0.062, 0.110, 0.139	0.012, 0.023, 0.042, 0.053	91.0, 90.8, 90.9, 90.9
IF	0.031, 0.062, 0.108, 0.139	0.0111, 0.022, 0.039, 0.050	88.7, 88.7, 88.7, 88.7

Table 4
Statistical temperature results for each configuration. Temperature values for 0.2 A/cm^2, 0.4 A/cm^2, 0.7 A/cm^2 and 0.9 A/cm^2, separated by commas for each parameter.

Configuration	T_{avg} (°C)	T_{std} (°C)	$T_{rel,max}$ (%)
NF	68.2, 67.9, 67.9, 67.4	0.114, 0.146, 0.266, 0.387	0.4, 0.4, 0.7, 1.2
IAF	68.2, 68.2, 67.8, 67.7	0.120, 0.157, 0.303, 0.336	0.5, 0.6, 1.1, 1.2
IHF	68.5, 67.9, 67.6, 66.9	0.101, 0.162, 0.288, 0.451	0.4, 0.5, 0.9, 1.5
IF	68.2, 68.5, 67.3, 66.9	0.118, 0.178, 0.356, 0.445	0.5, 0.7, 1.2, 1.5

density ratio was set to zero during the first 15 s of the test, then rapidly increased from 0 to 12.5% and maintained at this level for 13 s, and then, the current density ratio was rapidly decreased to 5% for 33 s. Afterwards, in a second zone, the transient evolution of the current density and voltage stick more significantly to the DLC current density ratio input. Within the urban driving cycle range, with low current density values below 0.26 A/cm^2, the NF configuration presented higher voltages compared to the other configurations, even though the IHF configuration had a higher current density value. For example, at t = 190 s the IHF configuration showed a voltage of 0.733 V at a current density of 0.256 A/cm^2, while at the same time the NF configuration reached a higher voltage of 0.753 V with a lower current density of 0.229 A/cm^2. Similar behavior but more pronounced differences were observed in the extra urban cycle, with current density values up to 0.898 A/cm^2. For example, at t = 1150 s, the IHF configuration showed a voltage of 0.550 V with a current density of 0.874 A/cm^2, and the NF configuration showed a higher voltage of 0.582 V with a lower current density of 0.781 A/cm^2.

Notwithstanding the above, as depicted in Fig. 11, the IHF configuration presented a higher power density curve, because the product of current density and voltage was higher for this configuration compared to the others for both urban and extra-urban driving cycle regions. In particular, the total energy density during the cycle for the IHF configuration at 210.6 J/cm^2 was in the range of 8.6–9.1% higher compared to the rest of configurations with energy densities in the range of 193–194 J/cm^2.

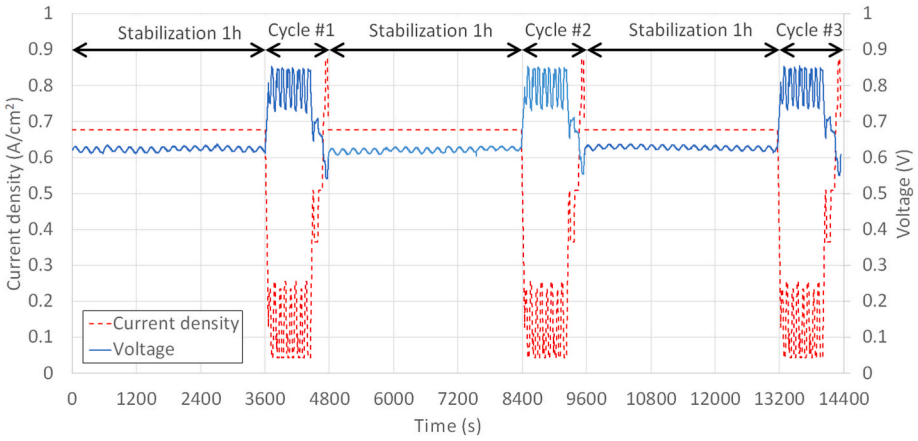

Fig. 9. DLC tests results of the IHF configuration.

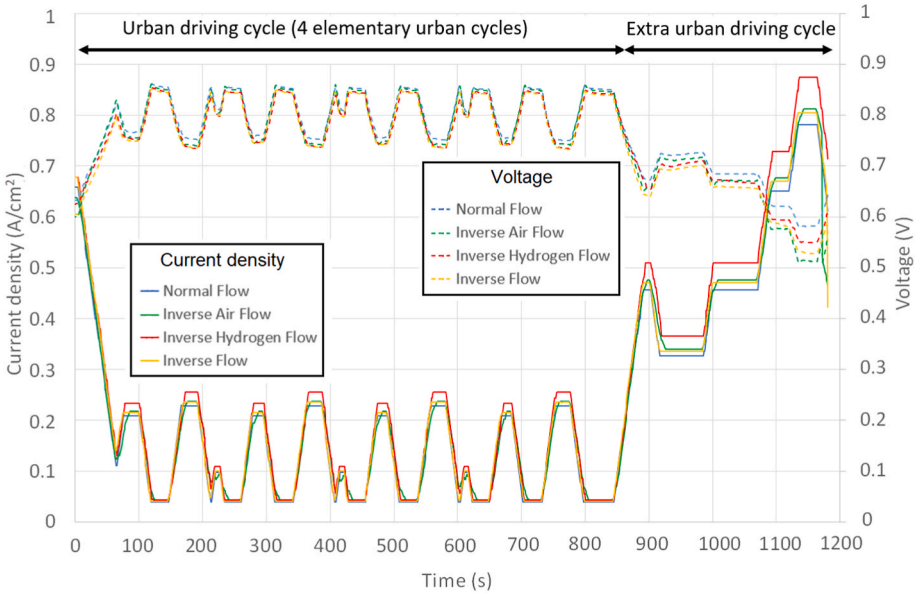

Fig. 10. DLC tests current density and voltage results of the different inlet/outlet configurations.

3.2.2. CDM measurements

CDM measurements were also performed during the DLC tests with a data acquisition rate of 1 s. As an illustrative example, the results for the IHF configuration can be visualized in video format as supplementary data in Appendix A, showing both current density and temperature distributions at every second of the DLC test.

To analyze the results obtained, Fig. 12 shows partial results for representative current densities of 0.2, 0.4, 0.7 and 0.9 A/cm^2 for the same IHF configuration. A total of five measurements were included in the analysis: two measurements at 0.2 A/cm^2 current density to compare the results during an increasing load variation (point 1) and a decreasing load variation (point 2), and one for each of the remaining current densities (points 3, 4 and 5). The scale in Fig. 12 has been fixed for the 5 points in to compare the results.

The statistical results of current density and temperature during DLC test are summarized in Table 5 and Table 6 respectively, for the representative points 1–5.

With respect to the current density distribution, similar to the previous CDM measurements for the polarization curve, the inverse bell-shaped distribution was observed in the five points analyzed. No significant differences in the CDM results were found when comparing the ascending (point 1) and descending (point 2) load variations. Although the inverse bell-shaped distribution was visually more pronounced at higher current densities (points 4 and 5), the maximum relative deviation from the current density average was approximately constant at all points, in the range of 78.9–79.6%. These percentages obtained were about 10% lower compared to the more heterogeneous distributions obtained during the polarization curves. Also, lower standard deviations were found during the DLC tests, especially in the high current density cases, indicating that the rapid changes in ascending and descending current densities caused less heterogeneity in the local current density distributions.

Regarding the CDM measurements for temperature, again very homogeneous distributions were observed, consistent with the previous CDM experiments of obtaining the polarization curve. No significant differences were found when comparing ascending (point 1) and descending (point 2) load variations. However, higher average temperatures with a maximum difference of 1.4 °C were found within the cell during the DLC tests in compared to the polarization curves.

4. Conclusions and research limitations

In this work, the performance of four different inlet/outlet configurations (Normal Flow, Inverse Oxygen Flow, Inverse Hydrogen Flow and

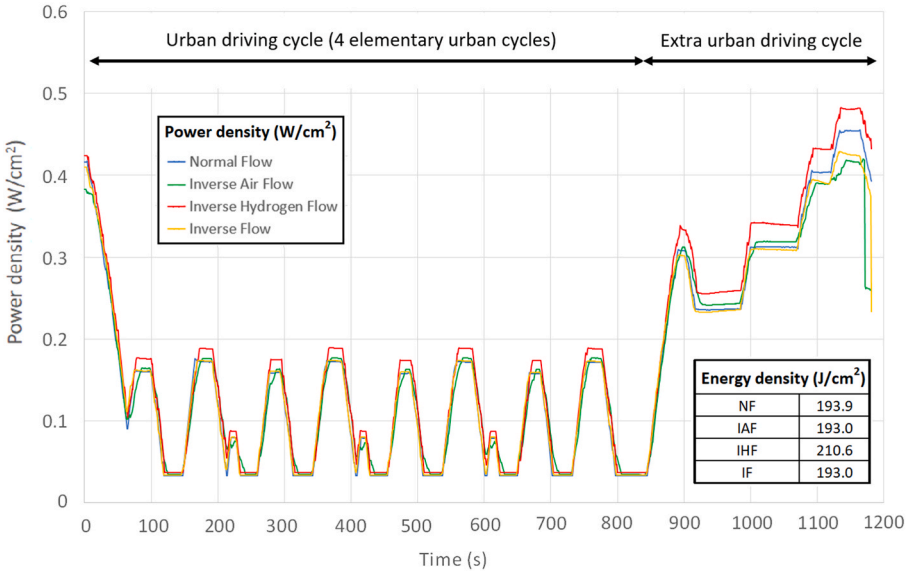

Fig. 11. DLC power density results of the different inlet/outlet configurations.

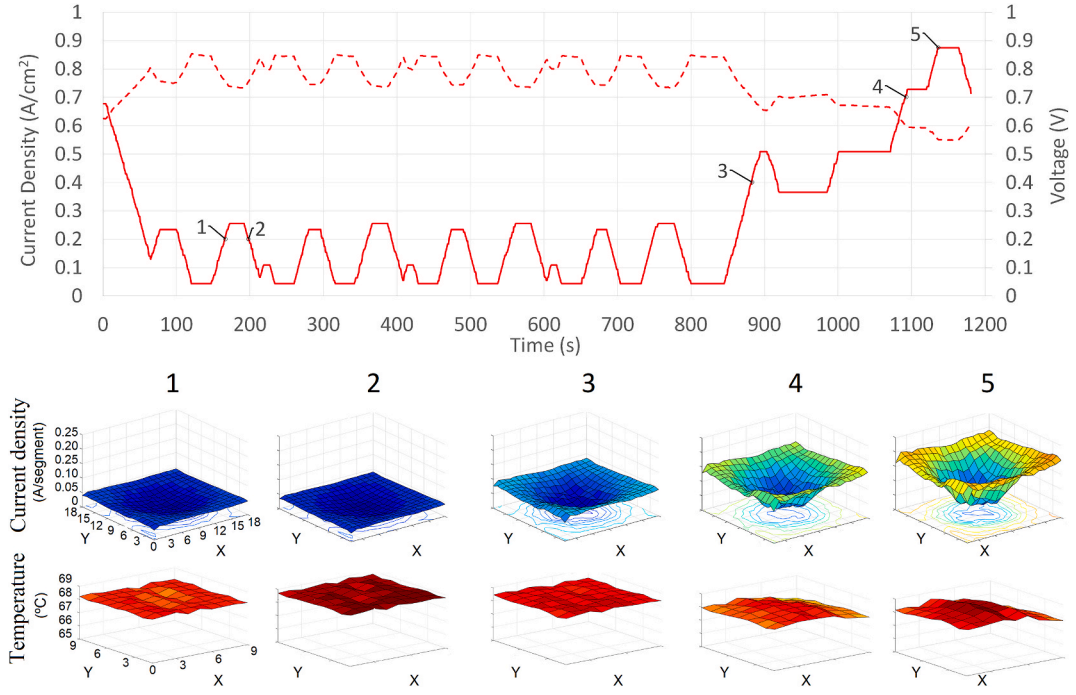

Fig. 12. CDM measurements during the DLC tests for IHF configuration.

Table 5
Inverse Hydrogen Flow (IHF) statistical current density results during DLC test. Current density values of points 1-5 separated by commas for each parameter.

Variable	$I_{d,avg}$ (A/cm^2)	$I_{d,std}$ (A/cm^2)	$I_{d,rel,max}$ (%)
Current density I_d	0.033, 0.030, 0.064, 0.110, 0.139	0.011, 0.010, 0.021, 0.036, 0.046	78.9, 78.9, 79.2, 79.2, 79.6

Table 6
Inverse Hydrogen Flow (IHF) statistical temperature results during DLC test. Temperature values of points 1-5 separated by commas for each parameter.

Variable	T_{avg} (° C)	T_{std} (° C)	$T_{rel,max}$ (%)
Temperature T	68.2, 68.8, 68.5, 68.1, 68.3	0.101, 0.097, 0.160, 0.294, 0.429	0.4, 0.3, 0.6, 1.1, 1.5

Inverse Flow) of a parallel-serpentine PEMFC was experimentally investigated. The experimental campaign included the determination of polarization and power curves, as well as dynamic load cycling tests to simulate real driving conditions with operating conditions that included fast variations in load, prolonged OCV exposure and periods of steady-state operation. CDM measurements of current density and temperature were taken during the experiments for both polarization and DLC tests. The key findings were:

- The IHF configuration performed best in terms of polarization and power curves. However, the differences with the other configurations were not significant, with maximum relative differences in power densities of less than 5% in compared to the other configurations.
- CDM measurements of the local current density showed significant heterogeneities in its distribution with maximum relative differences in the range 88–91%. An inverse bell-shaped distribution with higher current density values in the outer part of the bipolar plate and lower values in the central part was obtained for all configurations and current density values.
- CDM measurements of local temperature showed highly homogeneous distributions for all configurations and current density values, with maximum relative differences in the range 0.4–1.5%.
- The four proposed configurations were able to complete the dynamic load cycles, with correct cell behavior response. The IHF configuration performed best, with a total energy density during the cycle a 8.6–9.1% higher in compared to the rest of configurations
- When comparing the CDM measurements during the acquisition of the polarization curves and the DLC tests, no significant differences in the distributions were observed.

The results and conclusions obtained in this research were focused on the CDM measurements during the DLC tests for the proposed inlet/outlet configurations of a parallel serpentine 50 cm^2 single PEM fuel cell, and thus are applicable and valid within the context of the specific cases investigated. Due to the interrelationship and coupling of various physical phenomena such as complex interactions among species transport, fluid flow, porous media, heat transfer, electrochemical reactions, or electric current transport, the results cannot be directly extrapolated or generalized to other PEM fuel cell sizes, flow field configurations, operating conditions, or for the case of a stack of fuel cells. While further investigation of the aforementioned variables, as well as in-depth analyses of water management and membrane hydration levels, could provide additional insight and potentially refine the findings, presented results provide valuable information and solid foundation for understanding the temperature and current density measurements during a dynamic load cycling test.

Credir author statement

Christian Suárez: Methodology, Writing - Original Draft, Writing-Reviewing and Editing, Visualization. **Baltasar Toharias**: Investigation, Data curation. **María Salva Aguirre**: Investigation, Data curation. **Artem Chesalkin**: Writing- Original Draft. **Felipe Rosa**: Project administration, Funding acquisition. **Alfredo Iranzo:** Conceptualization, Methodology, Supervision.

Declaration of competing interest

The authors declare that they have no known competing financial interests or personal relationships that could have appeared to influence the work reported in this paper.

Data availability

Data will be made available on request.

Acknowledgements

Grant PID2019-104441RB-I00 funded by MCIN/AEI/10.13039/501100011033 and grant P20_01231 funded by PAIDI 2020 program by Junta de Andalucía, co-funded with ERDF funds. UNSE15-CE2962 and EQC2018-004258-P funded by MCIN/AEI, co-funded with ERDF funds. Authors would like to thank also the VII PPIT from the University of Seville and the Research, Technology and Innovation Centre (CITIUS) of the University of Seville.

Appendix A. Supplementary data

Supplementary data to this article can be found online at https://doi.org/10.1016/j.energy.2023.128455.

References

[1] Reddy KJ, Sudhakar N. ANFIS-MPPT control algorithm for a PEMFC system used in electric vehicle applications. Int J Hydrogen Energy 2019;44:15355–69.
[2] Chesalkin A, Kacor P, Moldrik P. Heat transfer optimization of NEXA Ballard low-temperature PEMFC. Energies 2021;14(8):2182. https://doi.org/10.3390/en14082182.
[3] Chu T, Zhang R, Wang Y, Ou M, Xie M, Shao H, Zhang C. Performance degradation and process engineering of the 10 kW proton exchange membrane fuel cell stack. Energy 2021;219:119623.
[4] Moldrik P, Chesalkin A, Minarik D. Infrared thermography and computer simulation in research of PEM fuel cells. 20th International Scientific Conference on Electric Power Engineering (EPE); 2019. p. 1–5. https://doi.org/10.1109/EPE.2019.8777969. 2019.
[5] Li Q, Liu Z, Sun Y, Yang S, Deng C. A review on temperature control of proton exchange membrane fuel cells. Processes 2021;9:235. https://doi.org/10.3390/pr9020235.
[6] Bisello A, Colombo E, Baricci A, Rabissi C, Guetaz L, Gazdzicki P, Casalegno A. Mitigated start-up of PEMFC in real automotive conditions: local experimental investigation and development of a new accelerated stress test protocol. J Electrochem Soc 2021;168(5). 10.1149/1945-7111/abf77b.
[7] Nguyen HL, Han J, Nguyen XL, Yu S, Goo YM, Le DD. Review of the durability of polymer electrolyte membrane fuel cell in long-term operation: main influencing parameters and testing protocols. Energies 2021;14(13):4048.
[8] Yang D, Tan Y, Li B, Ming P, Xiao Q, Zhang C. A review of the transition region of membrane electrode assembly of proton exchange membrane fuel cells: design, degradation, and mitigation. Membranes 2022;12(3):306. https://doi.org/10.3390/membranes12030306.
[9] Cullen DA, Neyerlin KC, Ahluwalia RK, Mukundan R, More KL, Borup RL, Weber AZ, Myers DJ, Kusoglu A. New roads and challenges for fuel cells in heavy-duty transportation. Nat Energy 2021;6:462–74. https://doi.org/10.1038/s41560-021-00775-z.
[10] Cho J, Kim H-S, Min K. Transient response of a unit proton-exchange membrane fuel cell under various operating conditions. J Power Sources 2008;185(1):118–28. https://doi.org/10.1016/j.jpowsour.2008.06.073.
[11] Kakati BK, Mohan V. Development of low-cost advanced composite bipolar plate for proton exchange membrane fuel cell. Fuel Cells from Fundamentals to Systems 2008;8(1):45–51. https://doi.org/10.1002/fuce.200700008.
[12] Yang G, Yu S, Kang Z, Dohrmann Y, Bender G, Pivovar BS, Green JB, Retterer ST, Cullen DA, Zhang FY. A novel PEMEC with 3D printed non-conductive bipolar plate for low-cost hydrogen production from water electrolysis. Energy Convers Manag 2019;182:108–16. https://doi.org/10.1016/j.enconman.2018.12.046.
[13] Bao C, Bessler WG. Two-dimensional modeling of a polymer electrolyte membrane fuel cell with long flow channel. Part II. Physics-based electrochemical impedance analysis. J Power Sources 2014;278:675–82. https://doi.org/10.1016/j.jpowsour.2014.12.045.
[14] Wilberforce T, Ijaodola O, Baroutaji A, Ogungbemi E, Olabi AG. Effect of bipolar plate material on proton exchange membrane fuel cell performance. Energies 2022;15(5):1886. https://doi.org/10.3390/en15051886.
[15] Hu B, He G, Chang F, Yang H, Cao X, Yin X. Low filler and highly conductive composite bipolar plates with synergistic segregated structure for enhanced proton exchange membrane fuel cell performance. Energy 2022;251:123982.
[16] Iranzo A, Arredondo CH, Kannan AM, Rosa F. Biomimetic flow fields for proton exchange membrane fuel cells: a review of design trends. Energy 2020;190:116435.
[17] Ke J, Wallace JS, Shu LH. Design improvements on a bipolar plate with passive water management using the biomimetic design method. In: ASME 2010 8th international conference on fuel cell science, engineering and technology; 2010. p. 833–41. https://doi.org/10.1115/FuelCell2010-33349.
[18] Hermann A, Chaudhuri T, Spagnol P. Bipolar plates for PEM fuel cells: a review. Int J Hydrogen Energy 2005;30(12):1297–302. https://doi.org/10.1016/j.ijhydene.2005.04.016.
[19] Zhang S, Xu H, Qu Z, Liu S, Talkhoncheh FK. Bio-inspired flow channel designs for proton exchange membrane fuel cells: a review. J Power Sources 2022;522:231003. https://doi.org/10.1016/j.jpowsour.2022.231003.
[20] Wang Y, Chen KS, Mishler J, Cho SC, Adrohera XC. A review of polymer electrolyte membrane fuel cells: Technology, applications, and needs on fundamental research. Appl Energy 2011;8(4):981–1007. https://doi.org/10.1016/j.apenergy.2010.09.030.
[21] Wang J. Theory and practice of flow field designs for fuel cell scaling-up: a critical review. Appl Energy 2015;157:640–63. https://doi.org/10.1016/j.apenergy.2015.01.032.
[22] Porstmann S, Wannemacher T, Drossela WG. A comprehensive comparison of state-of-the-art manufacturing methods for fuel cell bipolar plates including anticipated future industry trends. J Manuf Process 2020;60:366–83. https://doi.org/10.1016/j.jmapro.2020.10.041.

[23] Iranzo A, Muñoz M, López E, Pino J, Rosa F. Experimental fuel cell performance analysis under different operating conditions and bipolar plate designs. Int J Hydrogen Energy 2010;35:11437–47.
[24] Mingfu Y, Hong S, Tianyu Z, Qiang L, Jie L, Xiaochen Z. Current density distribution in an HT-PEM fuel cell with a poly (2, 5 – benzimidazole) membrane. Int J Hydrogen Energy 2021;46(3):3022–31. https://doi.org/10.1016/j.ijhydene.2020.04.117.
[25] Jia S, Liu H. Direct measurement of lateral current density distribution in a PEM fuel cell with a serpentine flow field. Int J Hydrogen Energy 2014;39(3):1449–56. https://doi.org/10.1016/j.ijhydene.2013.11.014.
[26] Shrivastava UN, Tajiria K, Chaseb M. Current density and ohmic resistance distribution in the land-channel direction of a proton exchange membrane fuel cell. J Power Sources 2014;299:189–94. https://doi.org/10.1016/j.jpowsour.2015.08.099.
[27] Higier A, Liu H. Optimization of PEM fuel cell flow field via local current density measurement. Int J Hydrogen Energy 2010;35(5):2144–50. https://doi.org/10.1016/j.ijhydene.2009.12.116.
[28] Mitzel J, Sanchez-Monreal J, Garcia-Sanchez D, Gazdzicki P, Schulze M, Häußler F, Hunger J, Schlumberger G, Janicka E, Mielniczek M, Gawel L. Fault diagnostic in PEMFC stacks by evaluation of local performance and cell impedance analysis. In: Fuel cells. From fundamentals to systems. 23rd EFCF conference "low-temperature fuel cells, electrolyzers, H2-processing forum" (EFCF2019). Switzerland: Lucerne; 2020. https://doi.org/10.1002/fuce.201900193. 2019.
[29] Miao T, Tongsh C, Wang J, Cheng P, Liang J, Wang Z, Jiao K. Current density and temperature distribution measurement and homogeneity analysis for a large-area proton exchange membrane fuel cell. Energy 2022;239:121922.
[30] Jiao K, Alaefour IE, Karimi G, Li X. Simultaneous measurement of current and temperature distributions in a proton exchange membrane fuel cell during cold start processes. Electrochim Acta 2011;56(8):2967–82. https://doi.org/10.1016/j.electacta.2011.01.019.
[31] Choi SR, Lim M, Kim DY, An WY, Lee SW, Choi S, Bae SJ, Yim S-D, Parka J-Y. Life prediction of membrane electrode assembly through load and potential cycling accelerated degradation testing in polymer electrolyte membrane fuel cells. Int J Hydrogen Energy 2022. https://doi.org/10.1016/j.ijhydene.2022.03.222.
[32] Han J, Han J, Yua S. Experimental analysis of performance degradation of 3-cell PEMFC stack under dynamic load cycle. Int J Hydrogen Energy 2020;45(23):13045–54. https://doi.org/10.1016/j.ijhydene.2020.02.215.
[33] Wang Y, Wang C-Y. Dynamics of polymer electrolyte fuel cells undergoing load changes. Electrochim Acta 2006;51(19):3924–33. https://doi.org/10.1016/j.electacta.2005.11.005.
[34] Mayur M, Strahl S, Husar A, Besslera WG. A multi-timescale modeling methodology for PEMFC performance and durability in a virtual fuel cell car. Int J Hydrogen Energy 2015;40(16):16466–76. https://doi.org/10.1016/j.ijhydene.2015.09.152.
[35] Tsotridis G, Pilenga A, De Marco G, Malkow T. EU harmonised test protocols for PEMFC MEA testing in single cell configuration for automotive applications. JRC Science for Policy report 2015;27632:21–3.
[36] http://www.splusplus.com. Accessed on June 23th, 2023.